LANGMUIR

pubs.acs.org/Langmuir Article

Simultaneous Detection and Photocatalysis Performed on a 3D Graphene/ZnO Hybrid Platform

M. Mercedes Messina, Marcos E. Coustet, Joaquín Ubogui, Remigio Ruiz, Fabio D. Saccone, P. Cecilia dos Santos Claro,* and Francisco J. Ibañez*

Cite This: *Langmuir* 2020, 36, 2231−2239 Read Online

ACCESS | Metrics & More | Article Recommendations | Supporting Information

ABSTRACT: The synergy between graphene foam (Gf) and ZnO nanoparticles (NPs) allows the detection of analytes at low conentrations, which can be subsequently photocatalyzed on the hybrid surface as well as in the liquid phase upon illumination with low-power UV−vis light-emitting diode (LED) lamps. Detection of methylene blue (MB) and bisphenol A (BPA) is monitored either by graphene-enhanced Raman scattering (GERS) or molecular doping/sensing upon analyte adsorption. Using GERS, we were able to detect concentrations as low as 0.3 ppm of MB, which remained adsorbed on the graphene surface after a photocatalytic conversion of 88% (total conversion). The photocatalysis performances of BPA and MB performed in the liquid phase were lower and corresponded to 73 and 33% as indicated by gas chromatography−mass spectrometry (GC/MS) and UV−vis, respectively. The kinetics of photocatalysis was fitted with a quasi-first-order reaction, and the apparent rate constant (k_{app}) was calculated according to the Langmuir−Hinshelwood model. The fastest kinetics was achieved with the hybrid platform named "Gf-ZnO400", which was thermally treated at high temperatures and with most of the Ni etched away. This is consistent with the excellent electronic interaction between ZnO and graphene foam as indicated by photoelectrochemistry analysis. We mainly employed Raman scattering and UV−vis spectroscopy analyses for detection and photocatalysis applications; however, we also used other complementary techniques such as focused ion-beam scanning electron microscopy (FIB-SEM), X-ray photoelectron spectroscopy (XPS), diffuse reflectance, GC/MS, and photoelectrochemistry to explore the synergetic behavior of these two nanomaterials. This work brings about new insights into the detection of analyte molecules followed by photocatalysis performed in the solid and liquid states.

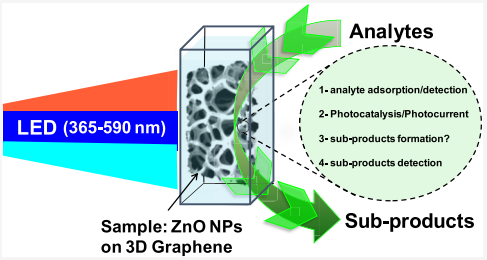

INTRODUCTION

The chemical synthesis of semiconducting nanoparticles (NPs) on three-dimensional (3D) graphene foams (Gf) brings about many benefits, which have been employed in optoelectronics,[1,2] Li-ion batteries,[3] supercapacitors,[4] electrochemical sensing,[5,6] environmental issues,[7] and more recently in photocatalysis.[8] Three-dimensional graphene has also been recently used as a precursor in the electrochemical synthesis of graphene quantum dots (GQDts).[9] There is a great interest in growing graphene on 3D structures because it offers much more area along with more divergent paths for electron collection and transport as compared to two-dimensional (2D) graphene. Besides, it has been demonstrated that chemical vapor deposition (CVD) graphene can grow on the entire surface of Ni catalysts.[10] Depending on the cooling rate, carbon atoms segregate to the surface, building up a monolayer or more frequently few- or multi-layers graphene (FLG or MLG).[11] During the growing process, the latter structure is arranged into two main types of stackings, which comprise AB and rotated layers whose physical and chemical properties are different as demonstrated theoretically,[12] experimentally by Weis et al. upon doping with ions,[13] and later by our group[14] upon molecule adsorption on the surface of graphene. Perhaps the most outstanding example could be the work of Cao et al., who demonstrated that if the angle of rotation between two graphene layers falls within the magic angle (∼1°), then superconductivity occurs.[15] In general, AB stacks behave more like graphite, whereas the rotated configuration behaves like monolayer graphene, although it may comprise several layers. Our group recently characterized in detail all of the possible stacking configurations that may be present on CVD graphene grown on Ni foams. We determined that both types of stackings led to graphene-enhanced Raman scattering (GERS);[16] however, the rotated configuration exhibited larger changes in the Raman bands every time the methylene blue (MB) analyte adsorbed on the surface.[14] Besides GERS, there is another phenomenon known as molecular doping, which causes changes in the characteristic Raman bands of graphene, mainly the G band, associated with electron exchange between

Received: November 11, 2019
Revised: February 10, 2020
Published: February 12, 2020

https://dx.doi.org/10.1021/acs.langmuir.9b03502
Langmuir 2020, 36, 2231−2239

adsorbed molecules and graphene.[17] Graphene is so sensitive to doping that it can reversibly sense UV-induced changes between cis- and trans-configurations in azobenzene molecules.[18] Therefore, graphene grown on Ni becomes an ideal hybridthat on one hand increases the Raman signal of adsorbed molecules, while on the other permits the detection of low analyte concentrations in a metal-free platform. If semiconducting NPs are grown on graphene, then photocatalysis under UV−vis light can be readily performed on the platform.

Photocatalysis usually requires a hybrid platform capable of charge separation and high electron transport to prevent electron−hole recombination once the light is turned on. There are several types of graphene-based semiconductors[19] and the most often employed ones correspond to metal oxide precursors (i.e., Zn^{2+})[20] or TiO_2 suspensions[21] in the presence of graphene oxide (GOx), which is later reduced to rGO by UV-assisted charge separation. The use of GOx as a building block in the formation of hybrids has been extensively employed likely because its functional groups promote sites for nucleation and growth of the metal ions, which ultimately leads to good chemical interaction between the nanocarbon and the semiconductor material. However, common drawbacks are associated with poor electron transport on rGO and a lack of control over the number of graphene layers, which tend to stack together via $\pi-\pi$ interactions while dispersed in a solution. The former issue is associated with defects and oxygen-containing functional groups that still remain even after the reduction of GOx.[22] Accordingly, it would be important to the growth of semiconducting nanoparticles on defect-free CVD graphene. This approach has been explored but usually requires a linker molecule to covalently attach the individual components.[23] There is a recent report that explores physical interactions via $\pi-\pi$ stacking between the analyte and graphene.[24] This approach is extremely useful for platforms composed solely of pristine graphene. Our approach, however, relies on a seedless synthesis, which follows a reaction where the OH groups from the solution attach to the defects of graphene (i.e., wrinkles). These defects later become active sites for the nucleation and growth of the semiconducting NPs.[25]

Here, we explore the synergy of 3D graphene and ZnO NPs toward the simultaneous detection and photocatalysis of these already detected analyte molecules. Photocatalysis is performed under UV−vis lights obtained from light-emitting diode (LED) lamps and monitored in both liquid- and solid-phase samples. Before growing the ZnO NPs, the Ni foam was partially removed to retain its stiffness and to achieve more illumination sites. The presence of graphene allowed the detection of low concentrations of MB and bisphenol A (BPA) via GERS and molecular doping/sensing, respectively. Due to GERS, we could monitor changes in concentration from 4 to 0.3 ppm measured after MB adsorption and during photocatalysis. Photocatalysis of MB was performed in the liquid phase and on the surface of the hybrid platform exhibiting 33 and 88% degradation of the analyte molecule, respectively. We also observed systematic shifts in the G band and changes in the intensity ratios between the 2D and G bands upon BPA adsorption on the platform. Since new Raman bands appeared during the photocatalysis of BPA, we complemented Raman with the GC/MS technique. New bands most likely correspond to benzaldehydes and esters that seemed to be formed during BPA degradation. More research is needed to further characterize the formation of subproducts during photocatalysis. Nevertheless, the conversion of BPA was 78% as measured by GC/MS. Photocurrent experiments performed on different platforms confirmed that Gf−ZnO400 hybrid samples possess an excellent performance under low-power UV−vis LED irradiation.

EXPERIMENTAL SECTION

Chemicals. Ethylenediamine (>99%), zinc nitrate hexahydrate (>98%), ammonium persulfate (>98%), sodium sulfate (99.9%), ethanol (200 proof), and acetone (>99%) were obtained from Sigma Aldrich. The nickel foam employed has a thickness of 1.6 mm and a porosity of 87%. Methylene blue (MB) and bisphenol A (BPA) were obtained from Merck. H_2 (99.999%) and CH_4 (99.999%) gases were purchased from Linde, Argentina. Nanopure water (17.8 MΩ·cm) was employed for all aqueous solutions.

Hybrid Platform. Graphene was grown on Ni foam by chemical vapor deposition (CVD) following parameters similar to those previously reported by our group[14] but this time keeping the vacuum pressure at 15 m Torr during the entire synthesis. As-grown graphene on Ni foam (NifG) was cut into 0.5 × 0.5 cm pieces and immersed for 2 days into a 1.0 M $(NH_4)_2S_2O_8$ etching solution prepared freshly every day and set to 70 °C. The product was then removed, rinsed in ethanol several times, and dried at 60 °C (Gf). ZnO nanoparticles (NPs) were grown by immersing the Gf sample into a mixture of 88 mM $Zn(NO_3)_2{\cdot}6H_2O$ and 178 mM $C_2H_8N_2$ at a controlled pH of > 10. The solution was set to 70 and 25 °C for 1 and 3 h, respectively, and the beaker was placed on a magnetic stirrer run at 300 rpm during the entire synthesis. The sample was then soaked in nanopure water and dried at 60 °C for 1 h. Finally, samples were annealed at 200 and 400 °C for 30 min.

Control Materials. The first control consisted of ZnO NPs grown directly on the Nif (without any source of graphene) following the same synthesis parameters as stated before. These samples were annealed at 400 °C for 30 min and namedNif−ZnO400. The second control sample consisted of a mixture of the same concentrations of $Zn(NO_3)_2{\cdot}6H_2O$ and $C_2H_8N_2$ in the absence of the Ni foam and any source of graphene. The precipitate at the bottom of the flask was then collected, grounded, and annealed at 400 °C (30 min). Finally, the sample was dispersed in ethanol, spin-coated on fluorine-doped tin oxide (FTO) glass, and placed in an oven at 200 °C for 1 h. This sample was named the ZnO powder.

Characterization. Raman spectra were acquired in a Jasco NRS-4100 microspectrometer, equipped with a 900 g/mm grating and an edge filter. The excitation beam was provided by a 20 mW power green laser at 532.34 nm. Raman signals were collected using a 20 × objective (0.4 NA-Olympus) at 100% laser intensity reaching ∼6.1 mW of power at the sample. A circular slit (d = 100 μm) was used and the acquisition time was 5 s for every five averaged spectra. A Si standard was used for wavenumber calibration. SEM images and energy-dispersive X-ray spectra (EDS) were acquired on FEI Scios 2. Cross-sectional images were acquired by ion-milling via the focused ion beam (FIB) technique. Diffuse reflectance measurements were carried out using a Shimadzu UV 2600/2700 spectrophotometer equipped with an integrating sphere. The equipment was calibrated with a $BaSO_4$ standard, and all measurements were collected using the standard as the background between 220 and 800 nm. To facilitate the analysis, all of the diffuse spectra were shown as "absorbance" plots. Photocurrent measurements were conducted in a three-electrode set-up placed in a commercial Zahner cell (PECC-2) connected to a multichannel potentiostat/galvanostat (Multi Autolab/M101). The platform was mounted on an FTO electrode along with reference (Ag/AgCl) and counter (Pt wire) electrodes immersed in 0.1 M Na_2SO_4 solution used as the electrolyte (see Figure S1 shown in the Supporting Information). The sample was exposed to two LED sources of 365 and 455 nm, which led to 10 and 40 mW/cm^2 light intensities at the sample, respectively. A distance of 3.5 cm was fixed between the working electrode and the light source. X-ray photoelectron espectroscopy (XPS) was run in ESPECS

https://dx.doi.org/10.1021/acs.langmuir.9b03502
Langmuir 2020, 36, 2231−2239

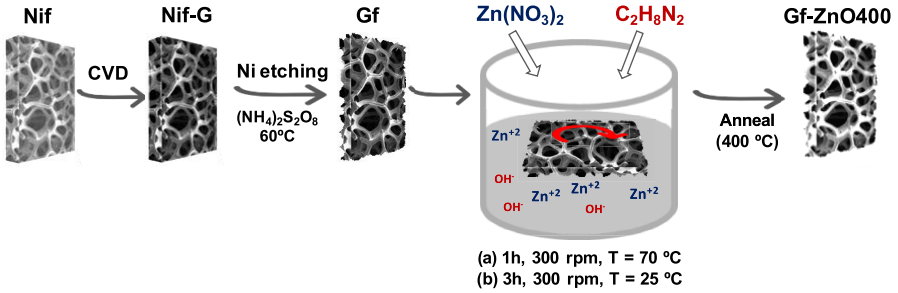

Figure 1. Scheme showing all of the steps involved in the synthesis of the hybrid platform, starting from growing graphene on Ni foam followed by the seedless synthesis of ZnO NPs on the graphene foam (Gf).

FlexMode system. XPS samples were mounted in a metallic hub with a conducting double-sided carbon tape. Measurements were performed using an AlKα monochromatic X-ray run at 100 W and 10 KeV with spot size of 3.5x1 mm^2 and pressure kept below $5x10^{-9}$ mbar.

Detection and Photocatalysis Performed on the Surface. Detection and photocatalysis were performed by keeping track of at least three different Raman spots before and after each experiment. The Raman intensity was reduced to 50% (~3 mW at the sample) to avoid laser-induced heating. Before immersion, samples were analyzed by Raman spectroscopy and then soaked in 1 mL of 20 ppm analyte solution for 30 min to provide enough time for adsorption. Samples were then removed, soaked in nanopure water, and dried at room temperature before performing the second set of Raman measurements. For the photocatalytic experiments, samples (with the already adsorbed analyte) were wetted with a drop of nanopure water and exposed to UV–vis LED irradiation for 30 and 60 min. Samples were placed with their front side toward the LED source (Thorlabs, LED4D067) coupled with a liquid light guide (Thorlabs, LED4D067) run at 365, 455, and 590 nm, which led to 0.48, 2.86, and 0.34 mW/cm^2 light intensities at the sample, respectively. The irradiance was measured with an optical power meter (Thorlabs, PM160T). Visible LED light at 660 nm whose wavelength is close to the absorbance band of MB (λ_{abs} = 664 nm) was excluded to avoid dye excitation.

Photocatalysis in the Liquid Phase. The sample was vertically immersed in a quartz cuvette containing 1 ppm MB in 3.4 mL of solution. The cuvette was then placed in the dark while stirring for 60 min to reach equilibrium and finally irradiated with LED lights. The distance between the platform and the light source was fixed at 4 cm. After reaching the adsorption–desorption equilibrium, the MB absorbance band at 664 nm was measured hourly to calculate the percent conversion during the experiment. GC/MS experiments for BPA were carried out in Perkin–Elmer 500/560D by injecting 1 μL of the sample into a column heated at a 10 °C/min ramp up to 270 °C final temperature.

RESULTS AND DISCUSSION

Building the Hybrid Architecture. Figure 1 shows a scheme of the step-by-step procedure to achieve the hybrid platform named Gf–ZnO400. First, graphene is grown on Ni foam by chemical vapor deposition (CVD) followed by the dissolution of Ni. Since we chose not to use poly(methyl methacrylate) (PMMA) as a support on as-synthesized 3D graphene,[26] we noticed that longer dissolutions times (more than 3 days) caused the collapse of the Ni scaffold, preventing further sample manipulation. The platform was then placed in a beaker, which remained floating, and spanned at 300 rpm for the entire synthesis. The synthesis of ZnO nanoparticles (NPs) follows a reaction where the OH groups attach to the defects of graphene (i.e., wrinkles), which later perform as nucleation sites for growing ZnO NPs.[25] Ethylenediamine forms a complex with Zn^{+2}, which readily reacts with OH groups attached to the surface of Gf.[27] The subsequent decomposition leads to the growth of ZnO on the surface of graphene foam.

Figure 2A,B shows SEM images along with a bar chart depicting the percent content of elements obtained by EDS.

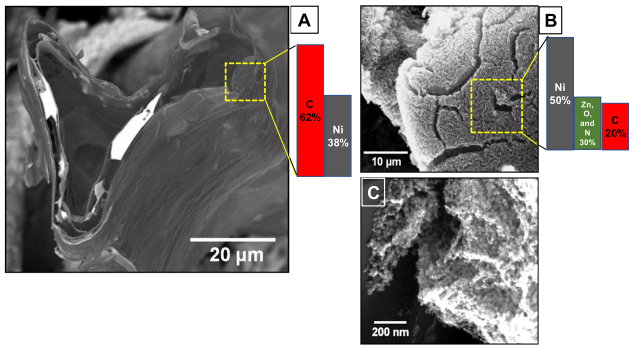

Figure 2. Cross-sectional SEM image obtained after placing a selected sample in the etching solution for 2 days (A). Different magnification SEM images of the as-prepared hybrid platform GfZnO400 (B, C). The center of the dotted line squares 1 and 2 are the spots subjected to EDS analysis. The bar chart shows the percent of elements found in these areas.

Figure 2A shows a cross-section SEM image obtained by ion-milling the graphene foam (after etching the Ni template). The structure exhibits bright spots and hollow areas. The former is associated with traces of Ni that still remain, whereas the latter corresponds to the ghost of the Ni foam, which seems to be surrounded by a few graphene layers. This correlates well with the literature[28] and our previous report,[14] which indicated that CVD graphene grows into multilayers forming different stacking configurations (vide infra). We found it necessary to complement SEM images with EDS analysis. For instance, the dotted square area marked in Figure 2A seems to be only graphene; however, EDS exhibited 32% Ni content. This clearly highlights the importance of combining both techniques. Figure S2 shows another cross-section SEM image from the same sample, which exhibits even larger amounts of Ni, indicating that the percent Ni content is area-dependent. Figures 2B and Figure S3 (Supporting Information) exhibit a uniform layer of ZnO NPs of ~20 nm diameter grown on the Gf surface along with an EDS analysis, respectively.

Figure 3 shows the Raman spectra of the ZnO powder used as a control, after etching of Ni (Gf), and after annealing the Gf–ZnO platform at different temperatures (200 and 400 °C). The Gf spectrum shows the characteristic G and 2D Raman spectra along with less intense bands corresponding to G* and

https://dx.doi.org/10.1021/acs.langmuir.9b03502
Langmuir 2020, 36, 2231–2239

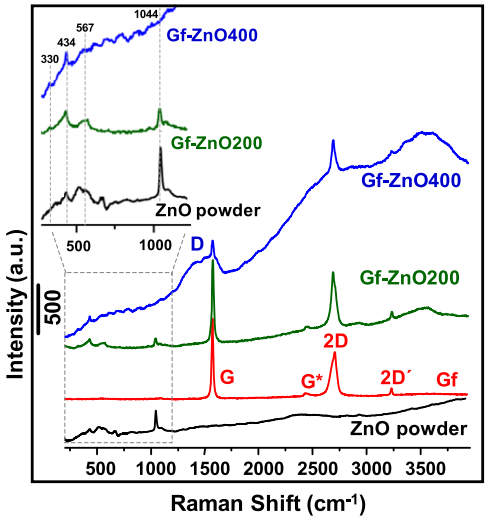

Figure 3. Representative Raman spectra measured for the selected ZnO powder (control), Gf (after Ni removal), Gf–ZnO annealed at 200 °C (control), and Gf–ZnO annealed at 400 °C (Gf–ZnO400). Raman spectra are off-set for better comparison.

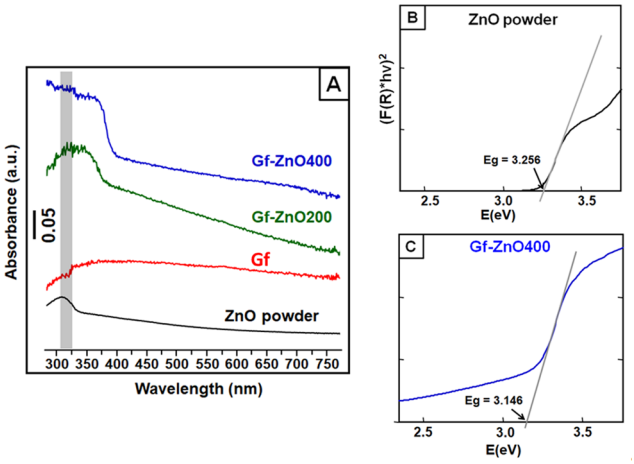

Figure 4. UV–vis absorbance spectra obtained by the diffuse reflectance technique measured for the selected ZnO powder (control), Gf (after Ni removal), Gf–ZnO annealed at 200 °C (control), and Gf–ZnO annealed at 400 °C named Gf–ZnO400 (A). The shaded stripes denote the adsorption edge of the ZnO powder. Tauc's plots correspond to the ZnO powder (B) and Gf–ZnO400 (C) and were obtained using the Kubelka–Munk (KM) function from the acquired diffuse reflectance in (A). The tangent line to the point of inflection on the curve is fitted, and the point of intersection of the tangent line and the horizontal axis corresponds to the E_g value. Spectra in (A) are off-set for better comparison.

2D′. Further Raman analysis of Gf exhibited the predominance of AB stacks, which is important to take into consideration since this type of piling has been shown to be less prone to changes in the characteristic Raman bands upon molecular doping (vide infra).[14] Although unknown, our results indicate that etching causes dramatic changes in the stacking configuration of graphene. Figure S4 confirms that the AB and rotated stacking configurations are present before Ni etching. Then, the growth of ZnO NPs on the surface of graphene can be assuredby the presence of its Raman bands located at 330, 434, 567, and 1044 cm^{-1}.[29] These bands, as expected, are also seen in the ZnO powder used as a control sample, whereas, for example, the band at 434 cm^{-1} corresponds to the $E2^{high}$ vibration mode characteristic of the wurtzita hexagonal phase of the ZnO crystal. Other bands located at 330, 567, and 1044 cm^{-1} correspond to second-order scattering, the A1 (LO) phonon mode, and the TO + LO mode, respectively. The Raman intensity and width indicate the degree of crystallinity of ZnO.[30] Unaffected Raman bands indicate that ZnO NPs grew on the graphene surface and that treatment at 200 °C caused no changes to the graphene structure whatsoever. However, the sample treated at 400 °C shows a sharp peak at 434 cm^{-1}, a low-intensity peak at 330 cm^{-1}, and the disappearance of the band at 567 cm^{-1}. The narrower 434 cm^{-1} band and the suppression of the band at 567 $cm^{-1}$are commonly associated with an improved crystallinity of ZnO NPs caused by annealing.[31,32] The Raman spectra of Gf also show changes after ZnO growth and annealing as noticed by the broad D band (defect band), which suggests the presence of carbon–oxygen sp^3 bonds.[33] Figure S5 shows a deconvolution of D and G bands after annealing at 400 °C. In conclusion, Raman spectra indicate that ZnO NPs coexist with Gf without damaging the overall graphene structure, yet increasing the number of defects as noted by the prominent D band.

Figure 4A shows UV–vis absorption spectra for the same samples shown in Figure 3. The shaded stripe represents the absorption wavelength edge for the ZnO powder located at ~380 nm. Whengraphene is grown and a part of the Ni is removed, the absorption edge shifts toward visible wavelengths (~410 nm) accompanied by an increase in the intensity of the entire visible range. Both the shift in wavelength and the increase in absorbance are consistent with the presence of graphene in the heterostructure, which also leads to changes in the energy band gap (E_g). Tauc's plots[34] shown in Figure 4B,C exhibit a decrease in the energy band gap (E_g) from 3.26 to 3.15 eV measured for Gf–Zn400 and ZnO powder samples, respectively.

Electronic Interaction between Graphene and ZnO. To further prove the interaction between the two nanomaterials, Figure 5A compares the evolution of the photocurrent density versus alternate "on" and "off" cycles of the UV LED light for the Gf–ZnO400 sample along with two other control samples indicated as Nif–ZnO400 and the ZnO powder. Figure S6 shows the photocurrent for the ZnO NPs alone. We wanted to compare samples with and without graphene upon photocurrent performance to determine the role of graphene in the platform. The figure exhibits a fast and stable photoresponse for the Gf–ZnO400 platform under 360 nm LED light whose current density reached a maximum at ~30 $\mu A/cm^2$. This value represents fourfold and more than 10-fold photocurrent enhancements as compared with Nif–ZnO400 and ZnO powder, respectively. It should be recalled that the ZnO powder was spin-coated on an FTO electrode (see Figure S1 for more details). The enhanced photocurrent for the Gf–ZnO400 sample can be attributed to the high electron mobility of graphene (arising from delocalized conjugated π-electrons) and the chemical interaction between G and ZnO (see the XPS analysis shown in Figure S7) crucial for separating electrons from holes and preventing recombination. When the sample is irradiated with UV light, the electrons in the valence band of the semiconductor get excited to the conduction band and then get injected into graphene due to its more positive Fermi level.[8] The potentials of the conduction and valence bands of ZnO are about −0.3 V and 3.1 V vs a normal hydrogen

https://dx.doi.org/10.1021/acs.langmuir.9b03502
Langmuir 2020, 36, 2231−2239

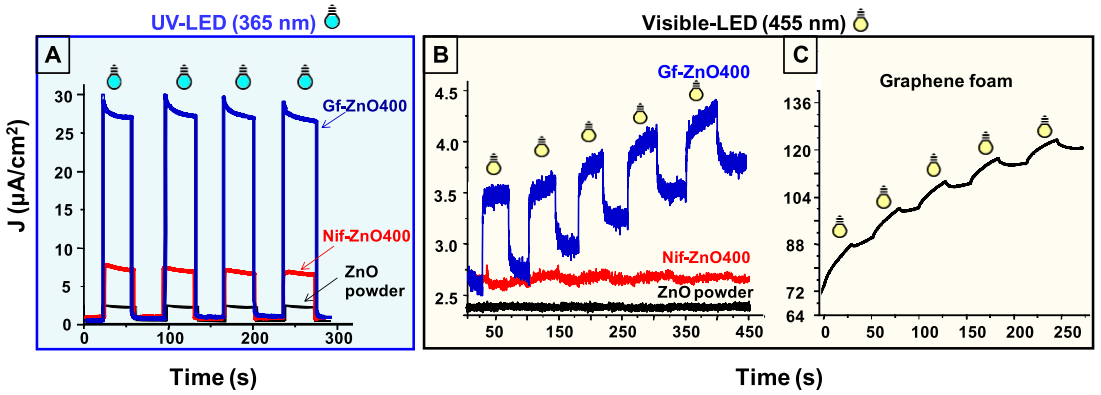

Figure 5. Current density (J) vs time (s) showing the photoresponse of the ZnO powder (control), Nif−ZnO400 (control), and Gf−ZnO400 hybrid samples exposed to UV light at 365 nm (A) and 455 nm (B). Photoresponse of graphene foam under LED visible light at 455 nm (C). All experiments were run at a bias voltage of 0 V (vs Ag/AgCl). [Na_2SO_4] = 0.1 M.

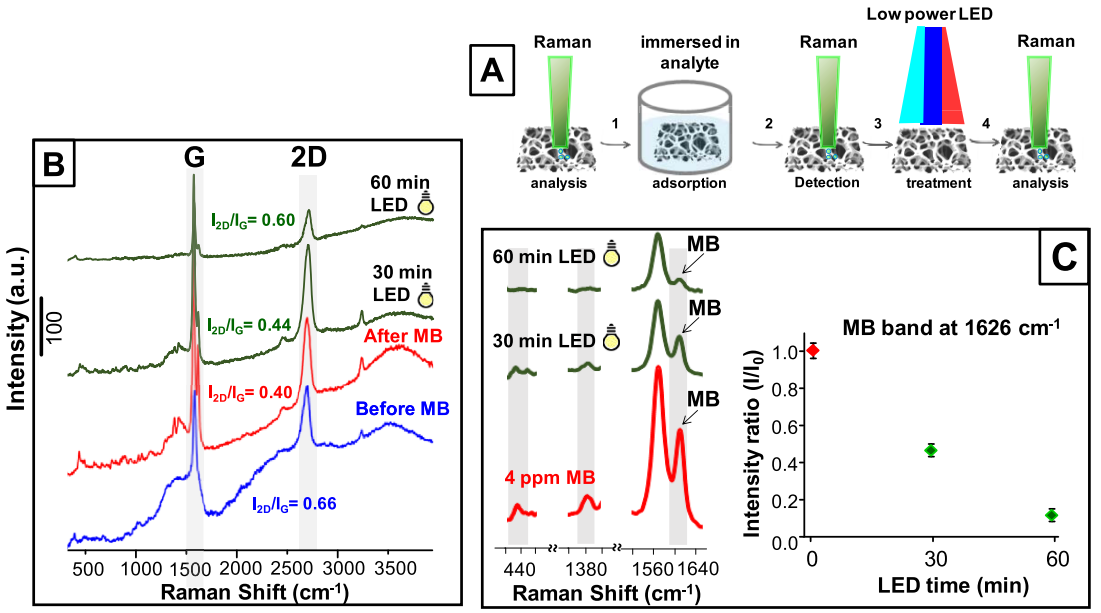

Figure 6. Representative scheme of all of the steps involved during the detection and photocatalysis performed on the hybrid surface (A). Selected Raman spectra of the Gf−ZnO400 sample before the adsorption of MB, after adsorption, and after UV−vis LED treatment for 30 and 60 min (B). The spectra show changes in the intensity ratio (2D/G) of the main Raman bands of graphene before and after adsorption and after treatment as indicated. Shaded areas denote the main Raman bands of graphene (B) and GERS of MB at 450, 1396, and 1626 cm^{-1}, respectively (C). Selected Raman spectra for the MB adsorbed on the platform and after 30 and 60 min irradiation times as indicated along with a plot that shows changes in the Raman Intensity (I/I_0) of the band located at 1626 cm^{-1} vs the irradiation time. Spectra are off-set for better comparison.

electrode (NHE), respectively, whereas for graphene, the potential is about 0.1 V vs NHE. These potential values make ZnO thermodynamically more favorable to transfer electrons to graphene.[35]

Figure 5B exhibits the photocurrent performance for the same samples as in Figure 5A but now exposed to visible LED light (455 nm). Although minimal, the presence of graphene increases the photocurrent. It also shows an anodic photocurrent response for both samples Gf−ZnO400 and Gf . It has been reported that under visible light, electrons in the Fermi level of graphene can be excited and transferred to the conduction band of the semiconductor, which could explain the photocurrent enhancement in graphene.[36]

Simultaneous Detection and Treatment on the Surface. Figure 6A shows a representative scheme of all of the steps involved during the detection and photocatalysis performed on the surface of Gf−ZnO400. The detection and LED treatment on the surface were carried out by keeping track of the same Raman spots before and after adsorption and after exposure to a low-power UV−vis LED light. Statistical analyses were performed on three to seven Raman spots before and after each experiment as indicated in the scheme. It is important to come back to the same spot since different stacking configurations and therefore different spectra/properties can be encountered within a few microns on the same sample (vide supra). Figure 6B shows Raman spectra before and after the adsorption of MB followed by 30 and 60 min of LED illumination. Figure 6C exhibits the spectra of MB before and after LED irradiation along with a plot of the intensity ratio (I/I_o) versus the irradiation time of the MB band located at 1626 cm^{-1}, respectively. The spectrum before absorption resembles that of an AB stacking, which is, unfortunately, a configuration less sensitive to molecular doping (vide supra); however, it still remains GERS active. This is remarkable since

https://dx.doi.org/10.1021/acs.langmuir.9b03502
Langmuir 2020, 36, 2231−2239

the concentration of MB on the surface is estimated to be only ~4 ppm (see Table 1). We also noticed systematic changes in the intensity ratio (I_{2D}/I_G) of the main Raman bands of graphene consistent with changes in the concentration of the adsorbed analyte[37] as indicated in Figure 6B and shown in Table 1. The table summarizes Avg. + STD based on changes in the intensity of MB bands, Avg. + STD intensity ratio (I_{2D}/I_G) measured from the main graphene bands (G and 2D) before and after MB adsorption and light irradiation, the concentration of the analyte on the surface, and the percent conversion during photocatalysis.

Table 1. Statistics for Changes in the Intensity of the MB Raman Band Measured at 1626 cm^{-1} and Changes in the Intensity Ratio (I_{2D}/I_G) of the Main Raman Bands of Graphene Measured Before and After Adsorption and After Irradiation under LED Lights[a]

Gf–ZnO400 sample	AVG + STD MB intensity measured at 1626 cm^{-1}	AVG + STD intensity ration (I_{2D}/I_G)	[MB] on the surface	Conversion (%)
Before MB		0.66 ± 0.03		
After MB	159 ± 4	0.40 ± 0.03	4 ppm[b]	0.0
30 min LED	74 ± 4	0.44 ±0.03	1.8 ppm	46.5
60 min LED	19 ± 5	0.60 ± 0.05	0.3 ppm	88.5

[a]Remaining concentration of MB on the surface and percent conversion upon photocatalysis. [b]Estimated concentration taken from the adsorption of MB on the surface after immersing the sample into a 20 ppm solution for 60 min (in the dark).

Figure 6C is a zoom-in from the spectrum of MB shown in Figure 6B, which exhibits GERS of the three characteristic Raman bands of MB at 450, 1396, and 1626 cm^{-1} (marked with shaded stripes) after adsorption and exposure to 30 and 60 min UV–vis LED. Only 60 min of irradiation is enough for the disappearance of two out of three of the MB Raman bands, while the intensity of the main band at 1626 cm^{-1} dramatically decreased as shown in the plot. This indicates that most of the adsorbed analyte was converted (~88%) within only 60 min of treatment with low-power LED light. Interestingly, the table indicates that the I_{2D}/I_G ratio is quite sensitive to changes in the analyte concentration. For instance, the ratio before absorption started at 0.66, then decreased to 0.44 (upon 4 ppm analyte adsorption), and finally reached 0.60 (0.3 ppm MB remaining), which is close to the initial value before adsorption. Since it never returned to the initial value (0.66), we may consider that some analyte still remains unconverted on the hybrid surface.

Unlike MB, we could not observe GERS of BPA likely due to the low concentration of the analyte, estimated to be ~2 ppm (see Table 2). However, we observed systematic shifts in the G-frequency band upon analyte adsorption and during photocatalysis as shown in Figure 7 and summarized in Table 2. Figure 7A shows two representative Raman spectra measured from the hybrid sample Gf-ZnO400 with already adsorbed BPA and after being subjected to UV–vis LED. The figure also shows the appearance of new bands at ~780 and ~1080 cm^{-1} marked with asterisks. It should be mentioned that these bands and others (spectra not shown) were occasionally observed. The inset exhibits a micro-Raman image of the evaluated spot.

Figure 7B shows selected spectra of the G band before and after BPA and after LED irradiation. The spectra exhibit a slight upshift after incubating the sample in BPA for 60 min in the dark. In contrast, after exposure to LED for 40/60 min, there is a systematic downshift of the G-band frequency. This phenomenon is known as molecular doping[37] and occurs when an electron-donating or -withdrawing analyte adsorbs on the surface. Although these shifts in the G-band frequency were marginal, and in some cases fall within the error of the instrument (±1.0 cm^{-1}), our statistics showed systematic and consistent upshifts every time the analyte adsorbed on the surface. Upshifts in the G band are attributed to p-doping in graphene as a consequence of electron withdrawing from the analyte molecules. On the other hand, downshifts were observed upon LED exposure in some cases exceeding the baseline value (1579 cm^{-1}). Overriding the baseline G-frequency (before analyte adsorption) may suggest that both (a) BPA is being degraded and/or (b) subproducts are being formed during LED illumination. The latter is consistent with the appearance of the new Raman bands shown in Figure 7A, whereas the former can be associated with BPA degradation as

Table 2. Average Frequency Shift (AVG) of the G Band, Shift Range of the G Band, AVG Changes in the Intensity Ratio (I_{2D}/I_G), Estimated Concentration of the Analyte on the Surface, Appearance of New Raman Bands, Assignment of these Bands, and GC/MS Analysis Before and After Irradiation with UV–Vis LED Lights[a]

Gf–ZnO400 Sample	AVG freq shift of G band (cm^{-1})	Range shift of G band (cm^{-1})	AVG change in intensity ratio (I_{2D}/I_G)	Estimated conc.BFA on the surface	New Raman bands (cm^{-1})	Raman bands assignments	% Conversion GC/MS[c]
Before BPA	1577	1577–1579	0.58				
After BPA	1580	1580–1581	0.78	2 ppm[b]	NO		
40/60 min LED	1577	1574–1578	0.61	U	2298		
					1080	COCN	
					1503		
					1149	RCOH	19
					787	RCOH	
120 min LED	N.M.	N.M.	N.M.	U	N.M.		73

[a]N.O. stands for "not observed", U stands for "unknown", and N.M. stands for "not measured". [b]Estimated concentration obtained from the adsorption of BPA on the surface after immersing the sample into a 20 ppm solution for 60 min. [c]% Conversion calculated by the area under the peak for BPA accounted from GC/MS experiments after 60 and 120 min of LED irradiation. ROCN, aliphatic carbodimines; RCOH, aldehydes; C=C, ethylenic bond.

https://dx.doi.org/10.1021/acs.langmuir.9b03502
Langmuir 2020, 36, 2231–2239

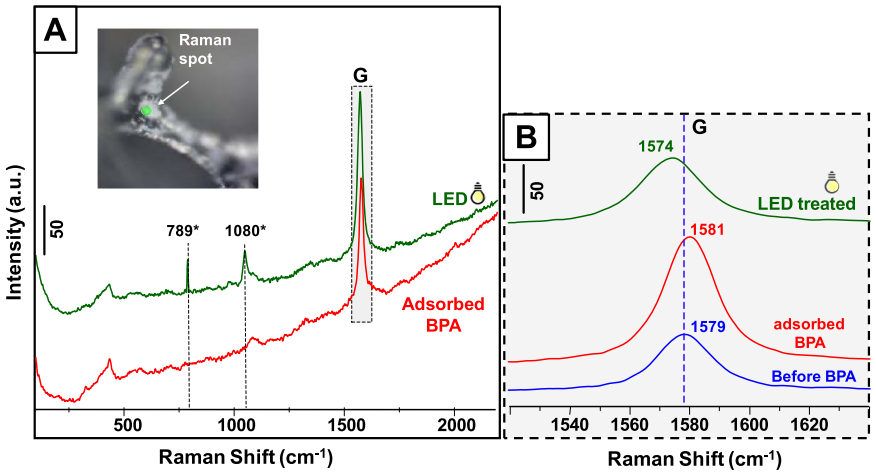

Figure 7. Representative Raman spectra of a selected Gf–ZnO400 sample after adsorption and treatment of BPA under UV–vis LED for 40–60 min along with the appearance of new Raman bands as indicated with * (A). The inset shows an optical image of the Raman spot corresponding to the spectra shown in (A). Selected Raman spectra before BPA adsorption, after BPA adsorption, and after 40/60 min LED treatment (B). Spectra are off-set for better comparison .

observed by GC/MS experiments that have shown 73% analyte degradation. Table 2 summarizes GC/MS and Raman information as indicated. The table shows reversible shifts in the G-frequency and the I_{2D}/I_G ratio taking into account the Raman measurements before analyte adsorption and after analyte conversion. This process has been observed by Gopalan and co-workers, who demonstrated reversible changes in Raman bands of pyridine molecules adsorbed on graphene upon alternating on and off cycles of UV light.[38] The table also shows potential assignments of Raman bands that may correspond to benzaldehydes and esters formed during photocatalysis. It is clear that more research is needed to further characterize the chemistry evolving at the interface; however, we demonstrated that changes in BPA can be simultaneously detected and photocatalyzed on the surface and in the liquid phase.

Photocatalysis of MB Performed in the Liquid Phase. We also monitored the photocatalysis of MB in the liquid phase by immersing the hybrid sample into a 1 ppm solution followed by 3 h of total exposure to low-power LED. Figure 8A,B shows the UV–vis absorption of the MB band measured at 624 nm along with a bar chart indicating the percent photocatalytic adsorption plus conversion during LED illumination. The plot shows a comparison against two controls (see Experimental Section for more details). As expected, the concentration of MB decreased with time under LED light irradiation. The first hour corresponded to the concentration at equilibrium (in dark) followed by 3 h of irradiation. The bar chart indicates the % AVG (adsorption + conversion) measured from three different samples. The Gf–ZnO400 sample reaches the highest value of 52%, which arises from the sum of adsorption (19%) plus conversion (33%) as compared to the other samples, which were treated at lower temperatures (Gf–ZnO200) and in the presence of the Ni scaffold (GNi–ZnO400). The kinetics of photocatalysis was fitted with the quasi-first-order reaction, and the apparent rate constant (k_{app}) was calculated according to the Langmuir–Hinshelwood model[39]

$$\ln\left(\frac{C_0}{C_t}\right) = k_{app} \cdot t$$

where C_0 and C_t correspond to the concentration of MB in the solution after 1 h in dark and the concentration at time t during the photocatalytic reaction, respectively. The highest k_{app} (4.0×10^{-3} min^{-1}) was achieved with the Gf–ZnO400 platform, whereas the values for GNi–ZnO400 and Gf–ZnO200 were 0.6×10^{-3} and 1.0×10^{-3} min^{-1}, respectively. Fast kinetics is consistent with the higher degree of analyte conversion for GNi–ZnO400, which can also be attributed to the number of defects and functional groups in graphene. In addition, removing a part of the Ni scaffold could also increase illumination sites on the 3D sample, thus improving the overall photocatalytic efficiency. It is important to note that photocatalysis performed in the liquid state resulted in a lower conversion demanding double the time under illumination as compared to the same analyte adsorbed on the surface ($k_{app} = 3.5 \times 10^{-2}$ min^{-1}). Finally, we evaluate the stability of the platform by subjecting the same sample to three consecutive photocatalysis . The total removal amounts of MB in the three successive cycles were 51, 48, and 47%, respectively, indicating that the Gf–ZnO400 platform has relatively good stability.

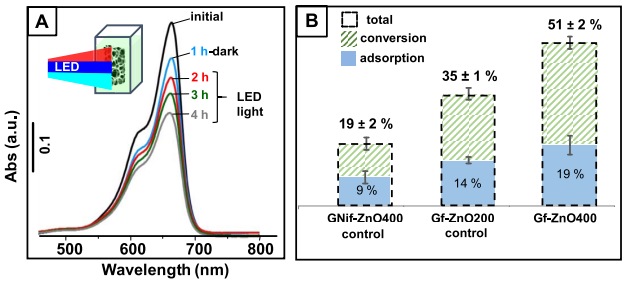

Figure 8. (A) Selected UV–vis spectra of the Gf–ZnO400 sample immersed in a 1 ppm MB solution. The spectra were obtained initially, after 1 h in the dark, and after 3 h of total exposure to low-power LED lights measured every hour. (B) Bar chart showing the adsorption and total (adsorption + conversion) percentage of MB for the three platforms GNi–ZnO400, Gf–ZnO200, and Gf–ZnO400 as indicated.

https://dx.doi.org/10.1021/acs.langmuir.9b03502
Langmuir 2020, 36, 2231–2239

CONCLUSIONS

We demonstrated that MB and BPA can be readily detected on the hybrid platform and later treated under low-power LED lamps to photocatalyze the adsorbed molecules. The detection of low analyte concentrations was carried by observing changes in the characteristic Raman bands of graphene consisting of either GERS or molecular doping. The former was achieved by observing the exalted Raman bands of the adsorbed analyte, whereas the latter was mainly monitored by systematic shifts of the G band as well as by changes in the intensity ratio (I_{2D}/I_G) of the main Raman bands of graphene. Photocatalysis occurs due to the presence of ZnO NPs within the heterostructure, and its efficiency was evaluated in the liquid and solid phases. We complemented Raman scattering and UV−vis spectroscopy analyses with other characterization techniques including FIB-SEM (and EDS), diffuse reflectance, XPS, GC/MS, and photoelectrochemistry to explore the synergetic behavior of these two nanomaterials. For instance, we were able to detect concentrations as low as 0.3 ppm of MB, which remained on the graphene surface after 88% conversion of the analyte. The analyte conversions of MB and BPA obtained in the liquid phase were 33 and 73%, respectively. The kinetics of photocatalysis was fitted with a quasi-first-order reaction, and the apparent rate constant (k_{app}) was calculated according to the Langmuir−Hinshelwood model. The fastest kinetics was achieved with the hybrid platform thermally treated at high temperatures and with a part of Ni etched away. We demonstrated a 10-fold photocurrent improvement for 3D graphene and ZnO NPs under UV LED light as compared to ZnO alone. We also noticed the emergence of a photoresponse under 455 nm visible-light irradiation. We believe that this work brings about interesting aspects regarding sensing and shooting performed at the interface of a hybrid platform comprised of 3D graphene and ZnO NPs.

ASSOCIATED CONTENT

Supporting Information

The Supporting Information is available free of charge at https://pubs.acs.org/doi/10.1021/acs.langmuir.9b03502.

(PDF)

AUTHOR INFORMATION

Corresponding Authors

P. Cecilia dos Santos Claro − *Gerencia de Investigación y Desarrollo, YPF Tecnología S. A., Berisso, Buenos Aires 1923, Argentina*; Email: cecilia.dossantos@ypftecnologia.com

Francisco J. Ibañez − *Instituto de Investigaciones Fisicoquímicas, Teóricas y Aplicadas (INIFTA), Universidad Nacional de La Plata - CONICET, La Plata 1900, Argentina*; orcid.org/0000-0003-0101-7667; Email: fjiban@inifta.unlp.edu.ar

Authors

M. Mercedes Messina − *Instituto de Investigaciones Fisicoquímicas, Teóricas y Aplicadas (INIFTA), Universidad Nacional de La Plata - CONICET, La Plata 1900, Argentina; Gerencia de Investigación y Desarrollo, YPF Tecnología S. A., Berisso, Buenos Aires 1923, Argentina*

Marcos E. Coustet − *Gerencia de Investigación y Desarrollo, YPF Tecnología S. A., Berisso, Buenos Aires 1923, Argentina*

Joaquín Ubogui − *Gerencia de Investigación y Desarrollo, YPF Tecnología S. A., Berisso, Buenos Aires 1923, Argentina*

Remigio Ruiz − *Gerencia de Investigación y Desarrollo, YPF Tecnología S. A., Berisso, Buenos Aires 1923, Argentina*

Fabio D. Saccone − *Gerencia de Investigación y Desarrollo, YPF Tecnología S. A., Berisso, Buenos Aires 1923, Argentina; Departamento de Física, Facultad de Ingeniería, Universidad de Buenos Aires, CABA 1963, Argentina*

Complete contact information is available at: https://pubs.acs.org/10.1021/acs.langmuir.9b03502

Notes

The authors declare no competing financial interest.

ACKNOWLEDGMENTS

We gratefully acknowledge financial support from PICT-2016-1377 and Cooperation Projects (CONICET-NSF) for student and professor exchange between the University of Louisville (KY, USA) and Universidad de La Plata. We also acknowledge Alejandra Floridia and Alberto Caneiro (Y-TEC) for FIB-SEM images and Jorge Andrés Donadelli, (Y-TEC) for XPS spectra. We would like to acknowledge Esther Svartman and María Mirífico (INIFTA) for carrying out GC/MS experiments.

REFERENCES

(1) Guo, Q.; Zhang, Y.; Zhang, H.-S.; Liu, Y.; Zhao, Y.-J.; Qiu, J.; Dong, G. 3D Foam Strutted Graphene Carbon Nitride with Highly Stable Optoelectronic Properties. *Adv. Funct. Mater.* **2017**, *27*, No. 1703711.

(2) Bonaccorso, F.; Sun, Z.; Hasan, T.; Ferrari, A. C. Graphene Photonics and Optoelectronics. *Nat. Photonics* **2010**, *4*, 611−622.

(3) Chang, Y.; Li, J.; Wang, B.; Luo, H.; He, H.; Song, Q.; Zhi, L. Synthesis of 3D Nitrogen-Doped Graphene/Fe3O4 by a Metal Ion Induced Self-Assembly Process for High-Performance Li-Ion Batteries. *J. Mater. Chem. A* **2013**, *1*, 14658.

(4) Dong, X.-C.; Xu, H.; Wang, X.-W.; Huang, Y.-X.; Chan-Park, M. B.; Zhang, H.; Wang, L.-H.; Huang, W.; Chen, P. 3D Graphene−Cobalt Oxide Electrode for High-Performance Supercapacitor and Enzymeless Glucose Detection. *ACS Nano* **2012**, *6*, 3206−3213.

(5) Yue, H. Y.; Huang, S.; Chang, J.; Heo, C.; Yao, F.; Adhikari, S.; Gunes, F.; Liu, L. C.; Lee, T. H.; Oh, E. S.; et al. ZnO Nanowire Arrays on 3D Hierachical Graphene Foam: Biomarker Detection of Parkinson's Disease. *ACS Nano* **2014**, *8*, 1639−1646.

(6) Dong, X.; Wang, X.; Wang, L.; Song, H.; Zhang, H.; Huang, W.; Chen, P. 3D Graphene Foam as a Monolithic and Macroporous Carbon Electrode for Electrochemical Sensing. *ACS Appl. Mater. Interfaces* **2012**, *4*, 3129−3133.

(7) Chen, N.; Pan, Q. Versatile Fabrication of Ultralight Magnetic Foams and Application for Oil−Water Separation. *ACS Nano* **2013**, *7*, 6875−6883.

(8) Cai, R.; Wu, J.; Sun, L.; Liu, Y.; Fang, T.; Zhu, S.; Li, S.; Wang, Y.; Guo, L.; Zhao, C.; et al. 3D Graphene/ZnO Composite with Enhanced Photocatalytic Activity. *Mater. Des.* **2016**, *90*, 839−844.

(9) Ananthanarayanan, A.; Wang, X.; Routh, P.; Sana, B.; Lim, S.; Kim, D.; Lim, K.; Li, J.; Chen, P. Facile Synthesis of Graphene Quantum Dots from 3D Graphene and Their Application for Fe3+ Sensing. *Adv. Funct. Mater.* **2014**, *24*, 3021.

(10) Li, X.; Cai, W.; Colombo, L.; Ruoff, R. S. Evolution of Graphene Growth on Ni and Cu by Carbon Isotope Labeling. *Nano Lett.* **2009**, *9*, 4268−4272.

(11) Yu, Q.; Lian, J.; Siriponglert, S.; Li, H.; Chen, Y. P.; Pei, S.-S. Graphene Segregated on Ni Surfaces and Transferred to Insulators. *Appl. Phys. Lett.* **2008**, *93*, No. 113103.

(12) Kim, K.; Coh, S.; Tan, L. Z.; Regan, W.; Yuk, J. M.; Chatterjee, E.; Crommie, M. F.; Cohen, M. L.; Louie, S. G.; Zettl, A. Raman Spectroscopy Study of Rotated Double-Layer Graphene: Misorientation-Angle Dependence of Electronic Structure. *Phys. Rev. Lett.* **2012**, *108*, No. 246103.

(13) Ek Weis, J.; Costa, S. D.; Frank, O.; Bastl, Z.; Kalbac, M. Fluorination of Isotopically Labeled Turbostratic and Bernal Stacked Bilayer Graphene. *Chem. - Eur. J.* **2015**, *21*, 1081−1087.
(14) Messina, M. M.; Picone, A. L.; dos Santos Claro, P. C.; Ruiz, R.; Saccone, F. D.; Romano, R. M.; Ibañez, F. J. Graphene Grown on Ni Foam: Molecular Sensing, Graphene-Enhanced Raman Scattering, and Galvanic Exchange for Surface-Enhanced Raman Scattering Applications. *J. Phys. Chem. C* **2018**, *122*, 9152−9161.
(15) Cao, Y.; Fatemi, V.; Fang, S.; Watanabe, K.; Taniguchi, T.; Kaxiras, E.; Jarillo-Herrero, P. Unconventional Superconductivity in Magic-Angle Graphene Superlattices. *Nature* **2018**, *556*, 43−50.
(16) Ling, X.; Xie, L.; Fang, Y.; Xu, H.; Zhang, H.; Kong, J.; Dresselhaus, M. S.; Zhang, J.; Liu, Z. Can Graphene Be Used as a Substrate for Raman Enhancement? *Nano Lett.* **2010**, *10*, 553−561.
(17) Dong, X.; Fu, D.; Fang, W.; Shi, Y.; Chen, P.; Li, L.-J. Doping Single-Layer Graphene with Aromatic Molecules. *Small* **2009**, *5*, 1422−1426.
(18) Peimyoo, N.; Li, J.; Shang, J.; Shen, X.; Qiu, C.; Xie, L.; Huang, W.; Yu, T. Photocontrolled Molecular Structural Transition and Doping in Graphene. *ACS Nano* **2012**, *6*, 8878−8886.
(19) Xiang, Q.; Yu, J.; Jaroniec, M. Graphene-Based Semiconductor Photocatalysts. *Chem. Soc. Rev.* **2012**, *41*, 782−796.
(20) Li, B.; Cao, H. ZnO@graphene Composite with Enhanced Performance for the Removal of Dye from Water. *J. Mater. Chem.* **2011**, *21*, 3346−3349.
(21) Williams, G.; Seger, B.; Kamat, P. V. TiO2-Graphene Nanocomposites. UV-Assisted Photocatalytic Reduction of Graphene Oxide. *ACS Nano* **2008**, *2*, 1487−1491.
(22) Díez-Betriu, X.; Mompeán, F. J.; Munuera, C.; Rubio-Zuazo, J.; Menéndez, R.; Castro, G. R.; de Andrés, A. Graphene-Oxide Stacking and Defects in Few-Layer Films: Impact of Thermal and Chemical Reduction. *Carbon* **2014**, *80*, 40−49.
(23) Park, J.; Jin, T.; Liu, C.; Li, G.; Yan, M. Three-Dimensional Graphene−TiO2 Nanocomposite Photocatalyst Synthesized by Covalent Attachment. *ACS Omega* **2016**, *1*, 351−356.
(24) Xu, J.; Wang, L.; Zhu, Y. Decontamination of Bisphenol A from Aqueous Solution by Graphene Adsorption. *Langmuir* **2012**, *28*, 8418−8425.
(25) Liu, J.; Lu, R.; Xu, G.; Wu, J.; Thapa, P.; Moore, D. Development of a Seedless Floating Growth Process in Solution for Synthesis of Crystalline ZnO Micro/Nanowire Arrays on Graphene: Towards High-Performance Nanohybrid Ultraviolet Photodetectors. *Adv. Funct. Mater.* **2013**, *23*, 4941−4948.
(26) Chen, Z.; Ren, W.; Gao, L.; Liu, B.; Pei, S.; Cheng, H.-M. Three-Dimensional Flexible and Conductive Interconnected Graphene Networks Grown by Chemical Vapour Deposition. *Nat. Mater.* **2011**, *10*, 424.
(27) Gao, X.; Li, X.; Yu, W. Flowerlike ZnO Nanostructures via Hexamethylenetetramine-Assisted Thermolysis of Zinc−Ethylenediamine Complex. *J. Phys. Chem. B* **2005**, *109*, 1155.
(28) Kozlova, J.; Niilisk, A.; Alles, H.; Sammelselg, V. Discontinuity and Misorientation of Graphene Grown on Nickel Foil: Effect of the Substrate Crystallographic Orientation. *Carbon* **2015**, *94*, 160−173.
(29) Dong, X.; Cao, Y.; Wang, J.; Chan-Park, B.; Wang, M.; Huang, L.; Chen, W. P. Hybrid Structure of Zinc Oxide Nanorods and Three Dimensional Graphene Foam for Supercapacitor and Electrochemical Sensor Applications. *RSC Adv.* **2012**, *2*, 4364.
(30) Honda, M.; Okumura, R.; Ichikawa, Y. Direct Growth of Densely Aligned ZnO Nanorods on Graphene. *Jpn. J. Appl. Phys.* **2016**, *55*, No. 080301.
(31) Aljawfi, R. N.; Alam, M. J.; Rahman, F.; Ahmad, S.; Shahee, A.; Kumar, S. Impact of Annealing on the Structural and Optical Properties of ZnO Nanoparticles and Tracing the Formation of Clusters via DFT Calculation. *Arabian J. Chem.* **2020**, *13*, 2207−2218.
(32) Yang, J.; Liu, X.; Yang, L.; Wang, Y.; Zhang, Y.; Lang, J.; Gao, M.; Feng, B. Effect of Annealing Temperature on the Structure and Optical Properties of ZnO Nanoparticles. *J. Alloys Compd.* **2009**, *477*, 632−635.
(33) Nan, H. Y.; Ni, Z. H.; Wang, J.; Zafar, Z.; Shi, Z. X.; Wang, Y. Y. The thermal stability of graphene in air investigated by Raman spectroscopy. *J. Raman Spectrosc.* **2013**, *44*, 1018−1021.
(34) Chen, Z.; Dinh, H.; Miller, E. *Photoelectrochemical Water Splitting: Standards, Experimental Methods, and Protocols*; Springer Briefs in Energy, Springer-Verlag: New York, 2013.
(35) Xu, J.; Cui, Y.; Han, Y.; Hao, M.; Zhang, X. ZnO−Graphene Composites with High Photocatalytic Activities under Visible Light. *RSC Adv.* **2016**, *6*, 96778−96784.
(36) Tang, B.; Chen, H.; Peng, H.; Wang, Z.; Huang, W. Graphene Modified TiO2 Composite Photocatalysts: Mechanism, Progress and Perspective. *Nanomaterials* **2018**, *8*, No. 105.
(37) Dong, X.; Fu, D.; Fang, W.; Shi, Y.; Chen, P.; Li, L.-J. Doping Single-Layer Graphene with Aromatic Molecules. *Small* **2009**, *5*, 1422−1426.
(38) Kim, M.; Safron, N. S.; Huang, C.; Arnold, M. S.; Gopalan, P. Light-Driven Reversible Modulation of Doping in Graphene. *Nano Lett.* **2012**, *12*, 182−187.
(39) Liu, B.; Zhao, X.; Terashima, C.; Fujishima, A.; Nakata, K. Thermodynamic and Kinetic Analysis of Heterogeneous Photocatalysis for Semiconductor Systems. *Phys. Chem. Chem. Phys.* **2014**, *16*, 8751.

https://dx.doi.org/10.1021/acs.langmuir.9b03502
Langmuir 2020, 36, 2231−2239